Hindawi
Advances in Civil Engineering
Volume 2022, Article ID 4152841, 9 pages
https://doi.org/10.1155/2022/4152841

Research Article

Variation Pattern of the Stress-Strain Curve of Concrete under Multifactor Coupling

Haijian Xie[1] **and Henglin Lv**[2,3]

[1]*School of Naval Architecture and Civil Engineering, Jiangsu University of Science and Technology (Zhangjiagang), Zhangjiagang, Jiangsu Province, China*
[2]*School of Mechanics and Civil Engineering, China University of Mining & Technology, Xuzhou, Jiangsu Province, China*
[3]*JiangSu Collaborative Innovation Center for Building Energy Saving and Construction Technology, Xuzhou, Jiangsu Province, China*

Correspondence should be addressed to Henglin Lv; henglinlu@yeah.net

Received 15 June 2022; Revised 26 July 2022; Accepted 27 July 2022; Published 18 August 2022

Academic Editor: Mehran Khan

The air shafts of coal mines contain solid, liquid, and gaseous substances that corrode concrete under conditions of relatively high temperature and humidity. The coupling of various factors decreases the concrete strength and thus the bearing capacity of the air shaft lining. In this study, concrete corrosion tests were carried out by simulating the complex environment of a coal mine air shaft lining to study the variation in the concrete stress-strain curve. For corroded concrete specimens subjected to very low stress, the microcracks and holes were closed, generating a large deformation, indicating severe concrete corrosion. The longer the corrosion time was, the gentler the initial slope of the curve. Finally, the uniaxial compression constitutive model of corroded concrete was established based on the Weibull distribution of three parameters, and the model curve was compared with the experimental curve. This model can not only predict the change of the stress-strain curve of high-strength concrete in a coal mine air shaft environment but also provide theoretical reference for the application of high-strength concrete in an air shaft environment.

1. Introduction

In coal mines, shafts are important channels through which coal is lifted and materials and personnel are transported during new well construction. Most deep mine shafts pass through a deep alluvium layer that is 500 to 1000 m thick or more. Air shafts are mainly used for ventilation. The deep thick alluvium layer is often rich in water, and the high-water pressure produces seepage, leaching, and leakage in most air shafts. Some groundwater contains ions that are corrosive to concrete (e.g., SO_4^{2-}) and therefore the shaft lining. During the mining process, coal mines release a large amount of CO_2 and gaseous media, such as HCl, that are corrosive to concrete. The mined coal also contains solid media that corrode concrete. The ventilation system allows gaseous, liquid, and solid media to pass through the air shaft. The long-term coupling effect of the high temperature and humidity conditions of the air shaft is the severe corrosion of the air shaft lining [1–4], thereby decreasing the concrete strength and the lining bearing capacity.

Thus far, many researchers have studied the durability of concrete. Yang et al. [5] studied the stress-strain constitutive relation and established a constitutive model for concrete in the saline soil region of western China under uniaxial compression. The effects of ion diffusion and chemical reaction were also discussed, and a mechanical analysis was performed. Zhou and Qiao [6] studied the tensile properties and elastic modulus of ultrahigh performance concrete (UHPC) under accelerated freeze-thaw cycles. Six series of UHPC specimens were tested by a well-designed direct tensile test (DTT) and the complete tensile stress-strain response was obtained. Araghi et al. [7] studied the properties of concrete containing 0%, 5%, 10%, and 15% PET particles as an alternative aggregate against sulfuric acid

corrosion. The study results showed that increasing the concrete PET particle content only slightly decreased the compressive strength, weight loss, and ultrasonic wave velocity of concrete. Cefis and Comi [8] investigated the mechanical properties of a concrete structure subjected to external sulfate attack under partially or fully saturated conditions. The relevant model was verified by simulating a scaled tunnel lining structure under an external sulfate attack. Chen et al. [9] and Zhou et al. [10] used a three-point bending test on concrete specimens to analyze the microscopic properties of cementitious materials that deteriorated under a simulated acid rain solution. The results of these studies showed that the deterioration of both cementitious materials and concrete specimens under acid rain attacks is mainly caused by the coupled effect of H^+ and SO_4^{2-}. Maes and De [11] studied the resistance performance of concrete and mortar against a combined attack of chloride and sodium sulfate. It can be concluded that chloride penetration increases when the sulfate content increases at short immersion periods, except for HSR concrete. Concerning the sulfate attack, the presence of chlorides has a mitigating effect. Wang et al. [12] examined the influence of acid rain corrosion on the fracture toughness of concrete and found that the concrete deterioration increased with time: a variation curve of the fracture toughness with the corrosion depth was produced. Sun et al. [13] conducted an experiment on the diffusion of sulfate ions in concrete. The experimental results were used to propose a novel diffusion model of sulfate ions considering the evolution of sulfate-induced conductive damage. Nie et al. [14] studied the strain produced in concrete under the coupled action of pressure and immersion in a sodium chloride and sodium sulfate solution. Dynamic tests were conducted on the specimens, and the test results were used in conjunction with statistical damage theory and the Weibull distribution to establish a stress-strain relation model of corroded concrete under dynamic statistical damage. Han et al. [15] used the relative dynamic elastic modulus to define the damage factor, establish the freeze-thaw damage model of tailings concrete based on Weibull distribution, and put forward the specific function form of two parameter Weibull distribution of iron tailings concrete under freeze-thaw cycle and used the model to predict its life. Xin et al. [16] studied the effect of dolomite powder on the freeze-thaw resistance of C30 and C45 concrete. Based on the Weibull distribution, a damage model of concrete containing dolomite powder is proposed. The research study shows that under the same freeze-thaw conditions, the damage degree of concrete treated with dolomite powder is lower than that of the reference sample. Tan et al. [17] compounded a silica fume and polyvinyl alcohol fiber in concrete and comprehensively analyzed and evaluated the strength change, mass loss, and relative dynamic elastic modulus change of concrete. The Weibull distribution probability model and GM (1, 1) model were established. The results show that both models can well reflect the development of concrete damage under a freeze-thaw environment.

The aforementioned studies have mostly focused on the properties of concrete materials or members under the action of one or two factors, whereas the environment of a coal mine air shaft lining is complex and subjected to the coupled action of multiple factors. In this study, concrete corrosion tests were carried out by simulating the complex environment of a coal mine air shaft lining to determine the mechanical properties of concrete. The statistical damage theory was used in conjunction with the Weibull distribution to establish a stress-strain curve for corroded concrete. The validity and feasibility of the method were verified using test curves. The model can not only predict the change of the stress-strain curve of high-strength concrete in coal mine air shaft environment but also provide a theoretical reference for the application of high-strength concrete in an air shaft environment.

2. Experimental Program

The dimensions of each of the concrete specimens used in this test were 100 mm × 100 mm × 300 mm. The concrete strength grade and a number of the concrete specimens are listed in Table 1. According to the on-site environmental sampling and testing results, it is found that the internal environment of the air shaft includes CO_2 (2655.4–6910.5 ppm), HCl (22.6–63.9 mg/m^3), and SO_4^{2-} (1554.33–3390.80 mg/l), which have a certain impact on the concrete [1–4, 18]. The natural environment of the air shaft was simulated in the test using the similarity theory based on the environmental characteristics of the air shaft. An artificial climate chamber was used to simulate the internal environment of the shaft lining, including the coupled environment of gaseous, liquid, and solid media and the temperature and humidity. A soak environment was used to simulate the external environment of the shaft lining. Table 2 shows the environmental conditions of the specimens. Figure 1 shows the artificial climate simulation and the test system.

Loading protocol: The complete stress-strain curve test of prismatic concrete blocks was carried out in the State Key Laboratory for Geomechanics and Deep Underground Engineering, China University of Mining and Technology. A YAS2000 electrohydraulic servo universal testing machine was used as the loading equipment. The loading was carried out according to the relevant protocol in the "Standard Test Method for Mechanical Properties on Ordinary Concrete" (GB/T 50081) [19], with a preload of 0.24 times the compressive strength, followed by loading at 0.01–0.02 mm/min.

3. Experimental Results and Analysis

3.1. Behavior under Applied Loading. The results of the uniaxial compression stress-strain test showed generally similar failure modes in corroded high-strength concrete prisms with different corrosion periods during the loading process, with the following differences. Prisms with a relatively short corrosion period and a relatively small extent of corrosion exhibited similar failure characteristics to those of an uncorroded prism member. However, for a prism that was corroded to a relatively large extent over a long corrosion time, a portion of the bottom edge of the specimen was crushed during the compression process and there were many tiny cracks in the crushed area. Before the load

Table 1: Types and number of concrete specimens.

Type	Concrete strength grade (standard curing for 28 days)	Number of groups	Remarks
1	C60	12	Three specimens in each group
2	C80	12	
3	C100	12	

Table 2: Settings for simulation of the natural environment inside and outside shaft lining.

	Environment settings					
Simulated position	Gaseous environment (ppm)	Acid mist environment (mg/m^3)	Saline rain environment (%)	Temperature and humidity environment	Test procedure	Time
Internal environment	CO_2/12,000	HCl/250	Na_2SO_4/10	Humidity 95%, temperature 40 ˚C	Gas injection by spraying two hours at a time, once every two days	45 days per cycle
External environment	–	–	Na_2SO_4/15	Humidity 100%, temperature 25 ˚C	Soak	

Na_2SO_4 concentration in mass percent.

Figure 1: Artificial climate simulation and system.

reached the peak compressive strength, no cracks were clearly visible on the surface of the high-strength concrete prism specimens. When the load reached the peak compressive strength, fine and short longitudinal cracks appeared on the specimen surface parallel to the long side of the specimen. At this time, several discontinuous longitudinal cracks continuously formed on the specimen surface. The prism specimen emitted a crisp sound while failing under loading, and the residual strength of the prism member disappeared. During the compressive failure process of some prism specimens, a main crack occurred in the diagonal direction. As the compression on the prism continued to increase, the first main crack propagated rapidly and continued to increase in width, while local crushing occurred at the bottom edge of some members. When the prism failed, this main crack penetrated through the entire specimen. The failure modes of some of the prism specimens are shown in Figure 2.

3.2. Experimental Stress-Strain Curve. It can be seen from the stress-strain curves in Figures 3 to 5 that the stress-strain curve of the uncorroded concrete is approximately linear before the peak stress [20, 21], whereas two regimes can be observed in the stress-strain curve of the concrete after corrosion before the peak stress. The first stage has a gentle slope, whereas the second stage is almost linear and resembles the stress-strain curve of the uncorroded concrete. At the beginning of compression, the concrete prisms with long corrosion times and relatively severe corrosion underwent large deformations even under relatively small stresses and the corresponding stress-strain curves had relatively gentle slopes. The results for high-strength concrete members with different corrosion periods show that the longer the corrosion time was, the gentler the slope of the initial curve, and the greater the strain under the same stress. Beyond a demarcation point, the slope of the curve suddenly increased approximately linearly, as in the rising section of the stress-strain curve of the uncorroded high-strength concrete prism, and the matrix of high-strength concrete was elastically compressed. When the stress of the high-strength concrete specimen approached the peak stress, a cracking sound was heard as the internal crack of the specimen propagated, but no macroscopic crack was visible on the specimen surface.

The gentleness of the curve slope before the demarcation point is attributed to microcracks and holes in the corroded concrete specimen. The longer the corrosion time of the concrete was, the more severe the corrosion, and the more microcracks and holes formed. Even under very low stress, the microcracks and holes in the specimen were closed, resulting in a large macroscopic deformation. The first section of the curve was very flat, and the maximum initial deformation occurred at a stress of approximately 1 to 2 MPa. In the second section of the curve, the slope suddenly increased and approached a constant value before 0.8 to 0.9 times the peak stress; then, the tangent modulus gradually decreased as the stress increased. Beyond the peak stress, the slope of the curve gradually decreased and started to change from positive to negative values. The plastic deformation of concrete began to increase. As the strain continued to increase, the curve became increasingly steep. At this point,

Figure 2: Shear failure as the major failure mode of prism specimens.

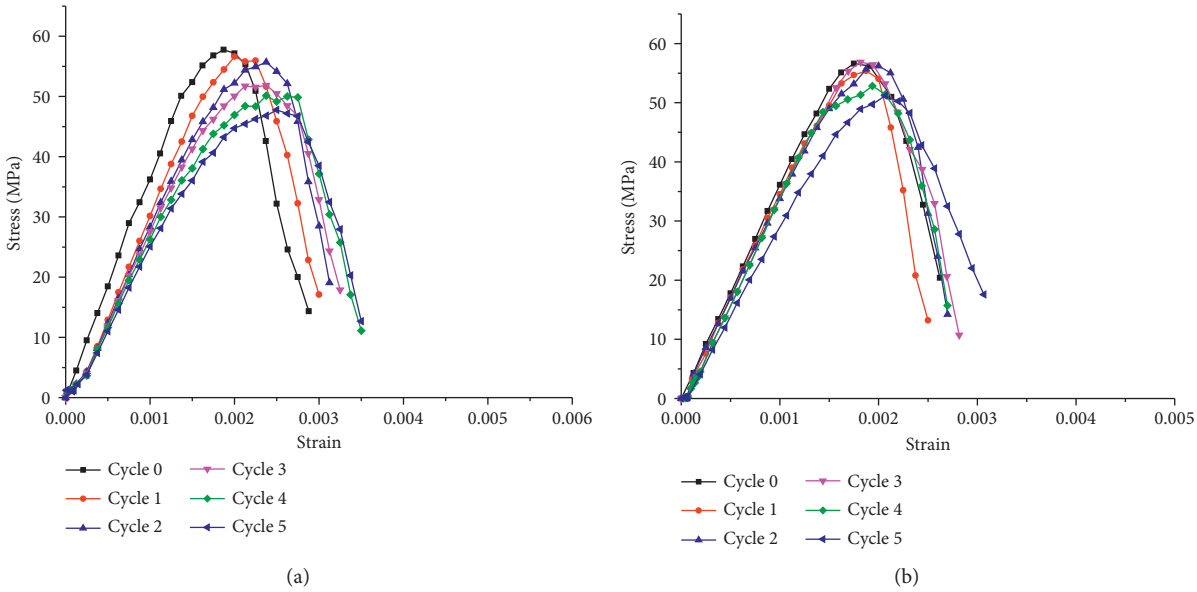

Figure 3: Stress-strain curves of C60 concrete. (a) Internal environment. (b) External environment.

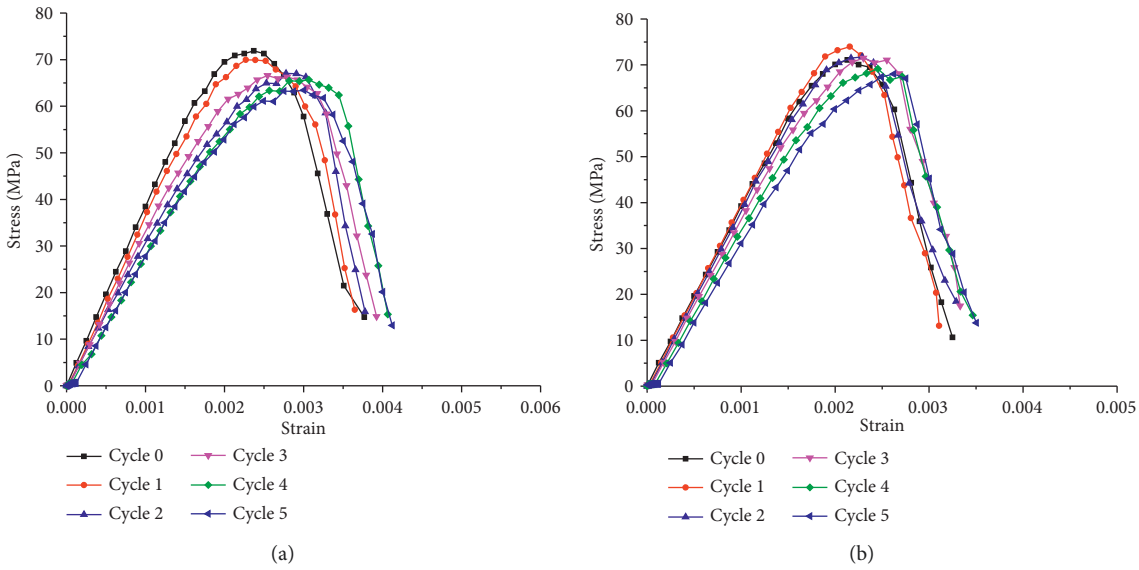

Figure 4: Stress-strain curves of C80 concrete. (a) Internal environment. (b) External environment.

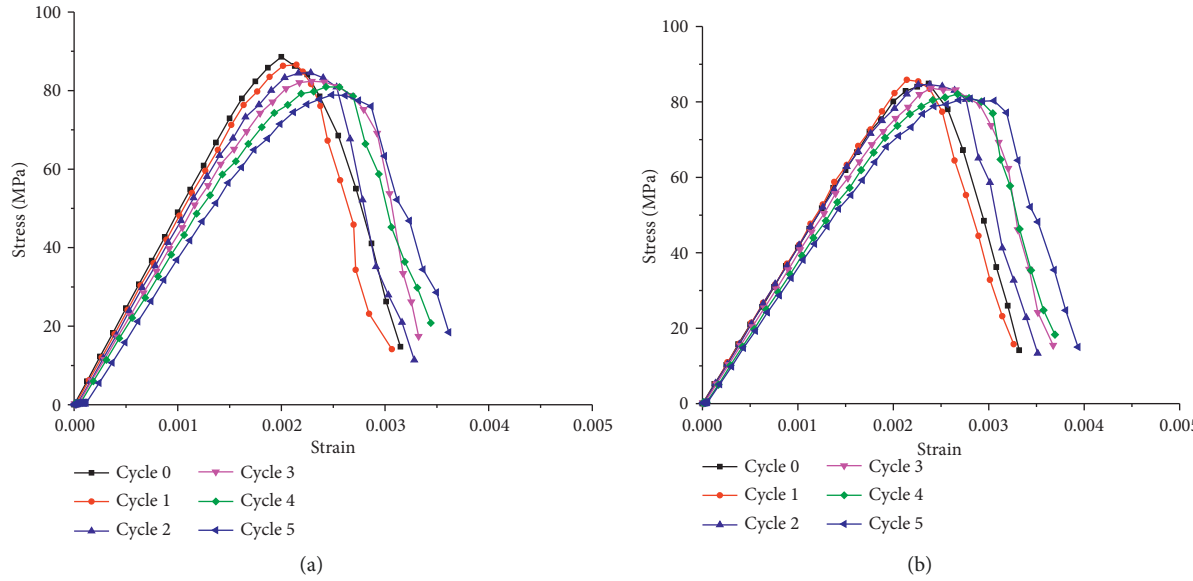

Figure 5: Stress-strain curves of C100 concrete. (a) Internal environment. (b) External environment.

each microcrack inside the concrete propagated independently without crossing or connecting with other cracks, and no macroscopic crack was found on the prism specimen surface. This stage was correspondingly denoted as steady-state microcrack propagation. As the displacement increased, new microcracks were generated at the interfaces of the coarse aggregates and cement mortar in the concrete specimen and developed rapidly. Prism cracking was heard intermittently. At this point, the internal microcracks widened and continuously propagated and converged into macrocracks on the concrete prism specimen surface. The first crack in the concrete prism specimen occurred in the middle portion of the specimen and was approximately parallel to the stress direction. The crack developed downward and diagonally as the displacement increased, and the residual concrete stress decreased rapidly.

3.3. Establishment of the Damage Model. The physical and mechanical properties of concrete are generally highly discrete. A very small amount of corrosion has a very small effect on the concrete physical and mechanical properties. In this case, it is very difficult to determine variations in the constitutive behavior by testing only a small number of specimens. When the concrete is corroded to a relatively large extent, the physical and mechanical properties of concrete are damaged to a much larger extent than in minimally corroded concrete, clearly reflecting the damage characteristics of the constitutive behavior of corroded concrete. The uniaxial stress-strain relations of corroded concrete exhibit both similarities and differences for different extents of corrosion. Although pure mathematical statistical models can be obtained for the corresponding corrosion periods by fitting test data, it is very difficult to establish a unified constitutive model [22–24]. In this study, relations for concrete with different corrosion periods and extents of corrosion are analyzed in conjunction with a relevant theory of damage mechanics to establish a uniaxial compression constitutive model of corroded concrete.

Concrete is a heterogeneous multiphase particle composite material formed by bonding coarse and fine aggregates with cementitious materials. Different mineral admixtures can also be used to produce high-strength concrete. Therefore, the composition and distribution of coarse and fine aggregates and cement paste in concrete is highly random. Here, concrete is considered to be composed of many tiny elements that are "macroscopically infinitesimal" and "microscopically infinite" at the same time. A "macroscopically infinitesimal" microelement is sufficiently small to be considered a particle in continuous damage mechanics, whereas a "microscopically infinite" microelement is sufficiently large to include the many microcracks and microdefects in the paste and at the interface. As a composite material, the concrete interior consists of many weak links of differing strengths, such that the strengths of microelements are also different. The fracture process of microelements in concrete has been reported to follow the Weibull distribution in many studies [25–28]. Based on continuous damage mechanics, the damage variable in this study is assumed to follow a three-parameter Weibull distribution, that is,

$$D = 1 - \exp\left[-\left(\frac{x - r}{\alpha}\right)^{\beta}\right], \tag{1}$$

where α is a scale parameter, $\alpha > 0$; β is a shape parameter, $\beta > 0$; and r is a position parameter, which can be considered as zero for stresses smaller than the peak stress.

In this study, the horizontal axis x reflects the strain, such that

$$D = 1 - \exp\left[-\left(\frac{\varepsilon - r}{\alpha}\right)^{\beta}\right]. \tag{2}$$

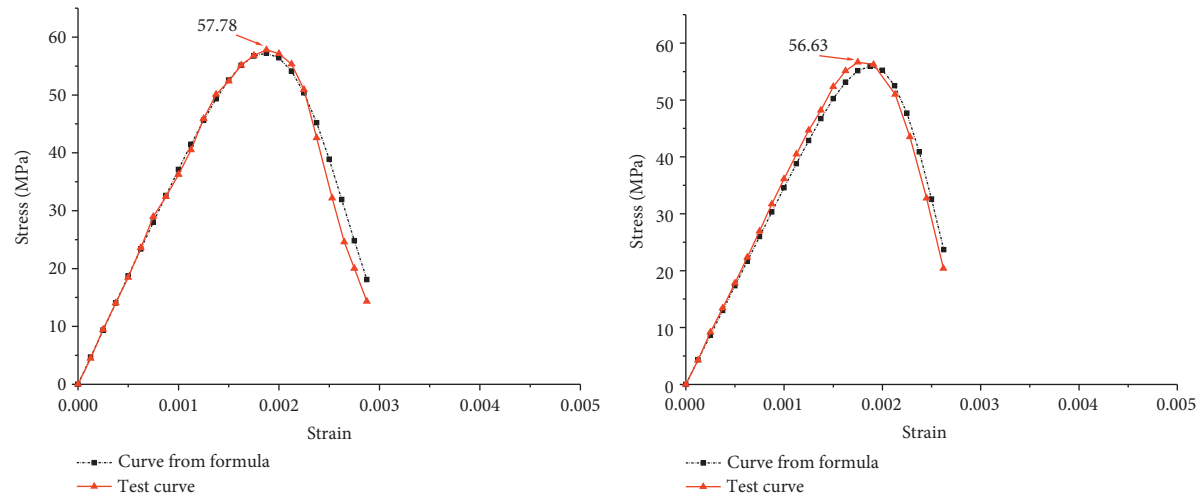

Figure 6: Comparison of test curves and curve from formula of C60 concrete. (a) Internal environment. (b) External environment.

From the theory of continuous damage mechanics, we have the following:

$$\sigma = E(1 - D)\varepsilon. \tag{3}$$

Substituting (3) into (2) yields as follows:

$$\sigma = E\varepsilon \exp\left[-\left(\frac{\varepsilon - r}{\alpha}\right)^{\beta}\right]. \tag{4}$$

Taking the derivative of the equation above yields as follows:

$$= E \exp\left[-\left(\frac{\varepsilon - r^{\beta}}{\alpha}\left[1 - m\left(\frac{\varepsilon - r}{\alpha}\right)^{\beta}\right]\right.\right]. \tag{5}$$

The initial conditions and geometrical conditions are as follows:

(1) $\varepsilon = 0, \sigma = 0$

(2) $\varepsilon = \varepsilon_{\mathrm{pr}}, \sigma = \sigma_{\mathrm{pr}}$

(3) $\varepsilon = \varepsilon_{pc}, d\sigma/d\varepsilon = 0.$

Then, we can obtain the following:

$$\beta = \frac{1}{\ln\left(E\varepsilon_{\mathrm{pr}}/\sigma_{\mathrm{pr}}\right)}. \tag{6}$$

Finally, substituting the value of αandβinto (4) yields the following:

$$\sigma = E\varepsilon \exp\left[-\frac{1}{\beta}\left(\frac{\varepsilon - r}{\varepsilon_{pc} - r}\right)^{\beta}\right], \tag{7}$$

where E is the tangent modulus corresponding to ε; ε_{pc} is the peak strain; β is a shape parameter; and E_{pr} is the secant modulus of the peak point passing through the point $\varepsilon_{\mathrm{pr}}$.

3.4. Outcome Comparison of Experimental Results and Damage Model. In this study, Origin software was used to fit the test data to determine the corrosion parameters. Formula (7) was used to obtain the uniaxial compressive stress-strain curve of the corroded concrete prism specimen, as shown in Figures 6 to 8. For clarity, only test curves and curves from the formula corresponding to periods 0 are compared in this study, with the understanding that the following discussion is also applicable to curves corresponding to the other periods. The parameter values of the curve for concrete are shown in Table 3. Refer to relevant papers [29, 30] and draw the standard deviation diagram of peak stress as shown in Figure 9.

It can be seen from Figure 8 that the stress-strain test curve obtained from the experimental data is in good agreement with the theoretically derived damage model curve before the peak stress, but after the peak stress, the experimental curve of concrete with strength grade C60 can be close to the damage model curve, and the experimental curve of concrete with strength grades C80 and C100 is quite different from the damage model curve. This indicates that for low-grade concrete, the damage model curve well fits the experimental curve before and after the peak stress; for concrete of high-strength grade, the damage model curve fits the experimental curve well before the peak stress but fits poorly after the peak stress.

Generally, the higher the strength grade of concrete is, the worse its ductility and plasticity will be. The difference occurring between the damage model curve and test curve after the point of inflection in the descending section of the stress-strain curve is mainly attributable to the switch of the deformation mechanism of the concrete specimen from fracture propagation to the slippage of the shear band when the strain exceeds the point of inflection in the uniaxial compression test of the concrete. In this case, the pressure on the specimen is mainly provided by the occlusal force caused by the friction on the slippage surface and the residual strength of small concrete cylinders divided by fractures. The concrete damage constitutive model in this study is established based on the theory of the parallel-bar system and Weibull distribution. It discretizes a volume

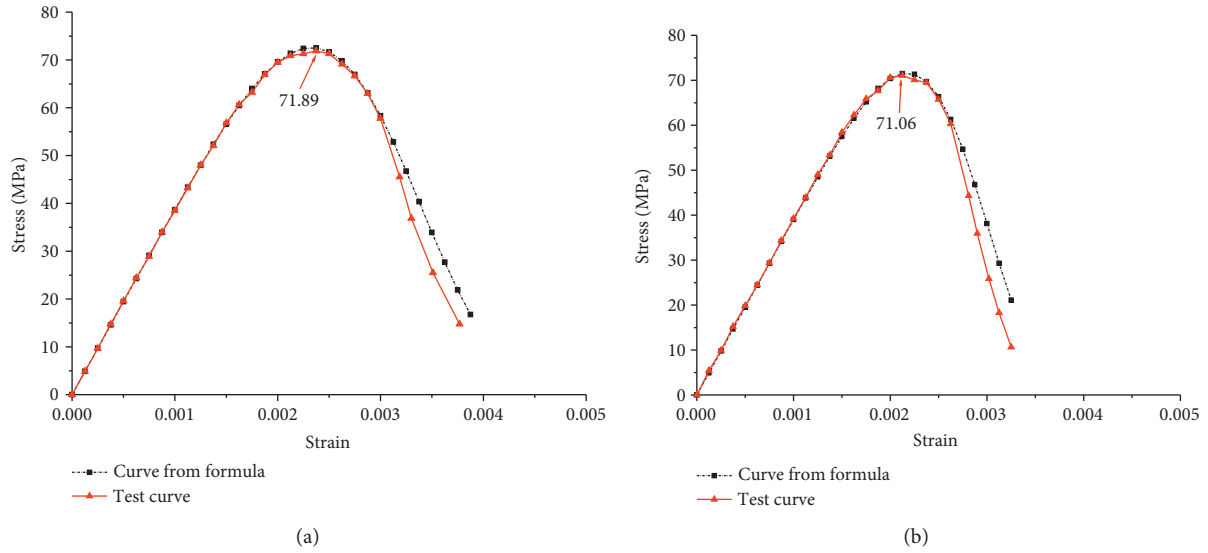

Figure 7: Comparison of test curves and curve from formula of C80 concrete. (a) Internal environment. (b) External environment.

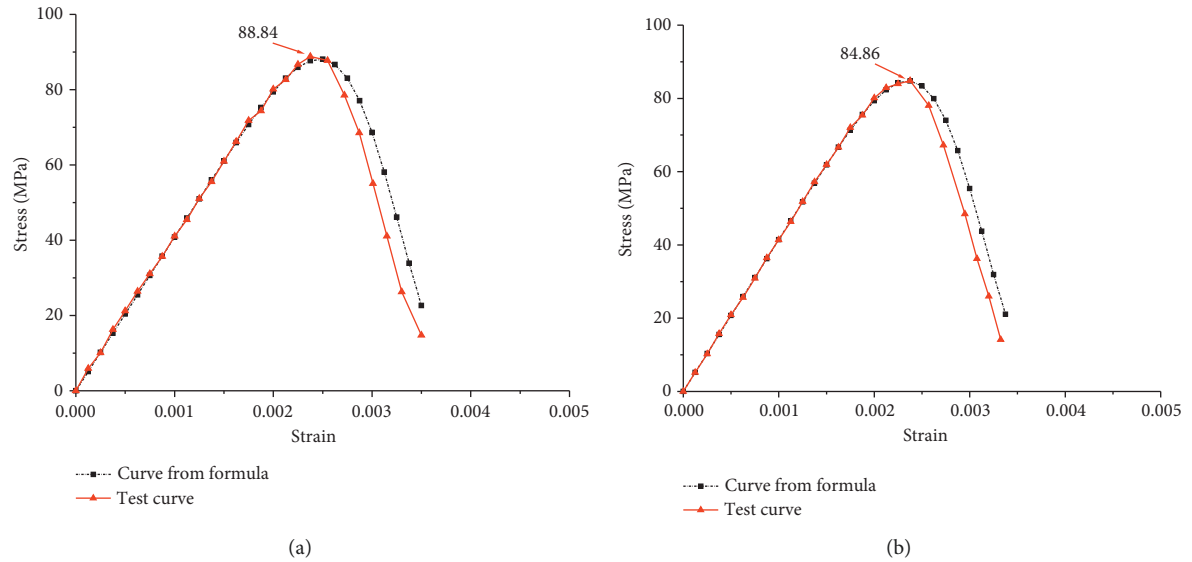

Figure 8: Comparison of test curves and curve from formula of C100 concrete. (a) Internal environment. (b) External environment.

Table 3: Every parameter value in the stress-strain curve of concrete (test curve).

Concrete strength grade	Environment	E ($\times 10^4$ MPa)	E_{pc} ($\times 10^4$ MPa)	σ_{pc}(MPa)	ε_{pc}
C60	Internal environment	3.59	3.09	57.78	0.00187
C60	External environment	3.44	3.24	56.63	0.00175
C80	Internal environment	3.92	3.03	71.89	0.00237
C80	External environment	4.33	3.34	71.06	0.00213
C100	Internal environment	4.74	3.75	88.84	0.00237
C100	External environment	4.16	3.58	84.86	0.00237

element into multiple parallel-bar elements and stimulates microscopic damage based on the fracture of bar elements. Meanwhile, because of the insufficient rigidity of the testing machine and that it is unable to apply strain (displacement) at a constant rate, concrete specimens with higher strength grades are rapidly destroyed, and the slope of the test curve increases rapidly. The experimental curve agrees poorly with the damage model curve.

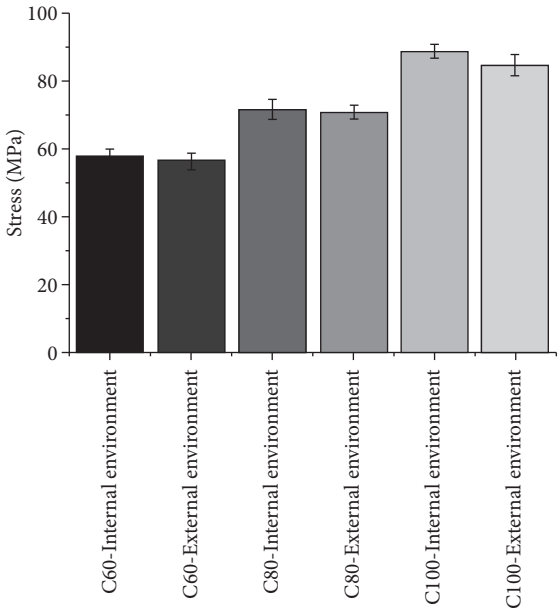

Figure 9: Standard deviation of peak stress.

4. Conclusions

In this study, the corrosion tests on concrete were conducted by simulating the complex environment in which the coal mine air shaft lining is located. The changes in stress-strain curves of concrete were investigated. A uniaxial compressive constitutive model of corroded concrete was constructed based on the three-parameter Weibull distribution, and the experimental results were compared with those of mathematical equations. The conclusions are as follows:

(1) A relatively short period and light degree of prism's corrosion results in the damage characteristics being basically the same as those of the uncorroded prism components; a relatively long period and severe degree of prism's corrosion results in partial crushing at the bottom edge of the components during the compression of the tested prism, with a huge amount of tiny cracks emerged at the crushing part.

(2) The conditions of the uniaxial compressive test process of the corroded prism are roughly the same as those of uncorroded high-strength concrete although some specialties exist. For the corroded concrete specimen, microcracks, and holes close under very small stresses and then produce a large deformation. The more severely the concrete is corroded, the more salient this phenomenon becomes. The longer the corrosion period, the flatter the slope of the initial curve. When passing a certain cut-off point, the curve grows in an approximately linear proportion.

(3) The uniaxial compressive constitutive model of corroded concrete was constructed based on the three-parameter Weibull distribution. The theoretical stress-strain curve of corroded concrete is similar to the test curve before the peak stress point. The deformation mechanism of the concrete specimen changes after the peak stress point. Under the influence of the stiffness of the testing machine, the test ends faster, with a steeper slope in the descending section.

For the corroded concrete, the corresponding uniaxial compressive stress-strain curves might be obtained as long as the parameters of corrosion are determined.

Data Availability

All data generated or analyzed during this study are included in this published article.

Consent

Written informed consent was obtained from individual or guardian participants.

Conflicts of Interest

The authors declare that they have no conflicts of interest.

Authors' Contributions

XHJ has carried out the physical test of concrete specimens and deduced the theoretical formula and was a major contributor in writing the manuscript. LHL has greatly helped in the basic principle of concrete performance degradation. All authors read and approved the final manuscript.

Acknowledgments

This study was funded by the Suzhou science and technology development plan (grant no. SNG2020052).

References

[1] W. Yuan-Zhou, L. Heng-lin, S. C. Zhou, and Z. N. Fanga, "Degradation model of bond performance between deteriorated concrete and corroded deformed steel bars," *Construction and Building Materials*, vol. 119, pp. 89–95, 2016.

[2] S. Zhou, H. Lv, and Y. Wu, "Degradation behavior of concrete under corrosive coal mine environment," *International Journal of Mining Science and Technology*, vol. 29, no. 2, pp. 307–312, 2019.

[3] Z. Fang, H. Lyu, Y. Wu, C. Zhao, B. Liu, and Z. Fang, "Study of the time-varying mechanical performance of reinforced concrete (RC) columns under to small eccentric loading in coal mining industry environment," *Zhongguo Kuangye Daxue Xuebao/Journal of China University of Mining and Technology*, vol. 43, no. n 5, pp. 800–807, 2014.

[4] X. Haijian and Lv Henglin, "Simulation of slightly degraded reinforced concrete shaft lining in thick topsoil," *Tehnički vjesnik – Technical Gazette*, vol. 27, no. 2, pp. 611–617, 2020.

[5] D. Yang, C. Yan, S. Liu, Ju Zhang, and Z. Hu, "Stress-strain constitutive model of concrete corroded by saline soil under uniaxial compression," *Construction and Building Materials*, vol. 213, pp. 665–674, 2019.

[6] Z. Zhou and P. Qiao, "Durability of ultra-high performance concrete in tension under cold weather conditions," *Cement and Concrete Composites*, vol. 94, pp. 94–106, 2018.

[7] H. Janfeshan Araghi, I. M. Nikbin, S. Rahimi Reskati, E. Rahmani, and H. Allahyari, "An experimental investigation on the erosion resistance of concrete containing various PET particles percentages against sulfuric acid attack," *Construction and Building Materials*, vol. 77, pp. 461–471, 2015.

[8] N. Cefis and C. Comi, "Chemo-mechanical modelling of the external sulfate attack in concrete," *Cement and Concrete Research*, vol. 93, pp. 57–70, 2017.

[9] M.-C. Chen, K. Wang, and Li Xie, "Deterioration mechanism of cementitious materials under acid rain attack," *Engineering Failure Analysis*, vol. 27, pp. 272–285, 20130.

[10] C. Zhou, Z. Zhu, Z. Wang, and H. Qiu, "Deterioration of concrete fracture toughness and elastic modulus under simulated acid-sulfate environment," *Construction and Building Materials*, vol. 176, pp. 490–499, 2018.

[11] M. Maes and N. De Belie, "Resistance of concrete and mortar against combined attack of chloride and sodium sulphate," *Cement and Concrete Composites*, vol. 53, pp. 59–72, 2014.

[12] Z. Wang, Z. Zhu, X. Sun, and X. Wang, "Deterioration of fracture toughness of concrete under acid rain environment," *Engineering Failure Analysis*, vol. 77, pp. 76–84, 2017.

[13] C. Sun, J. Chen, J. Zhu, M. Zhang, and J. Ye, "A new diffusion model of sulfate ions in concrete," *Construction and Building Materials*, vol. 39, no. SI, pp. 39–45, 2013.

[14] L. Nie, J. Xu, and E. Bai, "Dynamic stress-strain relationship of concrete subjected to chloride and sulfate attack," *Construction and Building Materials*, vol. 165, pp. 232–240, 2018.

[15] H. Jie, C. Fu, S. Liu et al., "Life Prediction of Iron Ore Tailings Concrete under Freeze-Thaw Cycle Based on Weibull Distribution," vol. 2022, Article ID 8028009, 2022.

[16] Z. Xin, Yu Luo, and Y. Wu, "An innovative material with strong frost esistance—concrete containing dolomite," *Powder. Materials*, vol. 15, no. 5, p. 1721, 2022.

[17] Y. Tan, Z. Xu, Z. Liu, and J. Jiang, "Effect of silica fume and polyvinyl alcohol fiber on mechanical properties and frost resistance of concrete," *Buildings*, vol. 12, no. 1, p. 47, 2022.

[18] H. J. Xie, "Study on Degradation Law and Life Prediction of RC Shaft Structure Mechanical Properties in Deep Thick Alluvium Environment," *China University of Mining and Technology*, vol. 268, 2016.

[19] GB/T 50081-2016, *Standard Test Method for Mechanical Properties on Ordinary Concrete*China, 2016.

[20] K. E. Loland, "Continuous damage model for load-response estimation of concrete. continuous damage model for load response estimation of concrete," *Cement and Concrete Research*, vol. 10, no. 3, pp. 392–492, 1980.

[21] M. T. Bassuoni and M. M. Rahman, "Response of concrete to accelerated physical salt attack exposure," *Cement and Concrete Research*, vol. 79, pp. 395–408, 2016.

[22] G. Long, He Liu, K. Ma, and Y. Xie, "Uniaxial compression damage constitutive model of concrete subjected to freezing and thawing," *Zhongnan Daxue Xuebao (Ziran Kexue Ban)/ Journal of Central South University (Science and Technology)*, vol. 49, no. 8, pp. 1884–1892, 2018.

[23] Xi Liu, T. Wu, and Y. Liu, "Stress-strain relationship for plain and fibre-reinforced lightweight aggregate concrete," *Construction and Building Materials*, vol. 225, pp. 256–272, 2019.

[24] D. Saini and B. Shafei, "Concrete constitutive models for low velocity impact simulations," *International Journal of Impact Engineering*, vol. 132, Article ID 103329, 2019.

[25] X. Weng, M. Zhu, J. Zhang, B. Yang, and J. Liu, "Bending mechanical properties research on prestressed airport concrete pavements," *Structural Concrete*, vol. 19, no. 6, pp. 2029–2039, 2018.

[26] J. J. Ortega, G. Ruiz, R. C. Yu et al., "Number of tests and corresponding error in concrete fatigue," *International Journal of Fatigue*, vol. 116, pp. 210–219, 2018.

[27] G. Murali, T. Indhumathi, K. Karthikeyan, and V. R. Ramkumar, "Analysis of flexural fatigue failure of concrete made with 100% coarse recycled and natural aggregates," *Computers and Concrete*, vol. 21, no. 3, pp. 291–298, 2018.

[28] X. Chen, C. Chen, Z. Liu, J. Lu, and X. Fan, "Compressive behavior of concrete under high strain rates after freeze-thaw cycles," *Computers and Concrete*, vol. 21, no. 2, pp. 209–217, 2018.

[29] M. Khan, M. Cao, and M. Ali, "Cracking behaviour and constitutive modelling of hybrid fibre reinforced concrete," *Journal of Building Engineering*, vol. 30, Article ID 101272, 2020.

[30] M. Khan, M. Cao, C. Xie, and M. Ali, "Effectiveness of hybrid steel-basalt fiber reinforced concrete under compression," *Case Studies in Construction Materials*, vol. 16, Article ID e00941, 2022.